Chinese Chemical Letters 34 (2023) 107628

Contents lists available at ScienceDirect

Chinese Chemical Letters

journal homepage: www.elsevier.com/locate/cclet

Branched core-shell a-TiO_2@N-TiO_2 nanospheres with gradient-doped N for highly efficient photocatalytic applications

Qingsong Zhang[a,*], Yang Xiao[b], Liu Yang[a], Yanjun Wen[a], Zhu Xiong[c,*], Lin Lei[a], Lin Wang[d], Qingyi Zeng[a,*]

[a] School of Resource & Environment and Safety Engineering, University of South China, Hengyang 421001, China
[b] School of Chemistry and Chemical Engineering, University of South China, Hengyang 421001, China
[c] Key Laboratory for Water Quality and Conservation of the Pearl River Delta, Ministry of Education, School of Environmental Science and Engineering, Guangzhou University, Guangzhou 510006, China
[d] Hunan Institute Of Traffic Engineering, Hengyang 421001, China

ARTICLE INFO

Article history:
Received 27 March 2022
Revised 7 June 2022
Accepted 20 June 2022
Available online 23 June 2022

Keywords:
TiO_2
Core-shell nanosphere
N doping
Gradient doping
Photocatalytic H_2 production

ABSTRACT

A branched core-shell nanosphere composed of an anatase TiO_2 (a-TiO_2) core and a TiO_2 nanobranch shell with gradient-doped N (a-TiO_2@N-TiO_2) is synthesized by a simple *in situ* doping method, in which mixed crystal anatase-rutile TiO_2 (ar-TiO_2) nanosphere is first prepared by oxidizing Ti using H_2O_2, and then is etched by $NH_3{\cdot}H_2O$ to form $(NH_4)_2TiO_3$ nanobranches, which is converted into a-TiO_2@N-TiO_2 following an ambient annealing process. The diameter of a-TiO_2 core is ~500 nm, and the thickness of N-TiO_2 branched shell is ~100 nm with gradually increased N concentration from the bottom to the edge. Ultra-thin amorphous coating layers on the branches are also observed. The morphology of the composites could be further tuned by the amount of $NH_3{\cdot}H_2O$, and its effect on the photocatalytic performance is also investigated. The optimized a-TiO_2@N-TiO_2 shows an outstanding hydrogen evolution rate of 308.1 μmol g^{-1} h^{-1} under air mass (AM) 1.5 illumination, and also exhibits highly active in photocatalytic degradation of various refractory organic pollutants, including organic dyes, phenols, antibiotics, and personal care products, with removal ratios higher than 96% after 2 h operation. This can be due to the gradient-doped N-TiO_2 nanobranches, which not only provide bending band structure and defect level derived from the N impurities and O vacancies, resulting the formation of n-n^+ heterojunctions to improve the charge separation, but also enhance the charge transfer at the liquid-solid interface due to the numerous nanobranches and amorphous coating layers.

Development of highly efficient photocatalytic materials for water splitting or eliminating organic pollutants has been considered to be one of the important investigative fields [1–3]. TiO_2 is regarded as an ideal photocatalytic material, thanks to its non-toxicity, outstanding stability, and low cost [4,5]. However, pure TiO_2 photocatalysts generally suffer from the fast recombination rate of photoexcited electrons and holes, and a large band gap energy (3.2 eV) that is excited by only ultraviolet light (~4% of sunlight) [6]. Therefore, it is still urgently needed to design and prepare novel TiO_2 based photocatalysts with enhanced separation efficiency of photoexcited electron/hole pairs and visible light response to meet the practical requirement.

Recently, nitrogen (N) doped TiO_2 has attracted a lot of attention due to its narrowed band gap [7–9]. In the N-doped TiO_2, there are two states of N, namely substitutional and interstitial (Schemes S1a and b in Supporting information). In the substitutional case (Scheme S1a), corresponding to an oxygen (O) atom replaced by a N at a regular lattice site, an impurity energy level (E_i) in N-doped TiO_2 is introduced, which just above the valence band maximum [10]. While, in the case of interstitial position (Scheme S1b), *i.e.* directly bounding to lattice oxygen, leading to a slightly higher E_i in the gap [10]. This indicates that the electronic structure of N in the N-doped TiO_2 is part of the energy levels (N 2p) of TiO_2, which can effectively narrow its band gap. Moreover, N doping can simultaneously introduce oxygen vacancies (V_o) in the lattice [10–12]. Due to the presence of two excess electrons in N atom, two Ti^{4+} cations can be reduced to Ti^{3+} cations, leading to the formation of V_o and defect level (Ti^{3+} 3d, E_d). According to the previous studies, the formation of Ti^{3+} is found to be about 0.8 eV

* Corresponding authors.
E-mail addresses: qingyizeng@usc.edu.cn (Q. Zhang), xiongzhu@gzhu.edu.cn (Z. Xiong), qszhang@usc.edu.cn (Q. Zeng).

https://doi.org/10.1016/j.cclet.2022.06.051
1001-8417/

below the conduction band minimum, which can also narrow the band gap of TiO_2 [10,13,14]. However, the narrowed band gap is also a "double-edged sword". Although the doping of N can effectively improve the visible light response of the TiO_2, the photogenerated electrons and holes can recombine more easily due to the increased defect sites.

It is noteworthy that the presence of N impurities and V_o can also decrease the Fermi level (E_F) of the TiO_2, resulting in the electron transfer from the pure TiO_2 to N-TiO_2 when combining them together [15]. After the equilibrium of E_F, the band structure will be bending and causing the formation of n-n^+ heterojunction [16], which can facilitate the transfer of electrons and holes to the N-TiO_2. In this case, constructing a core-shell structured TiO_2@N-TiO_2 photocatalyst will be favorable to enhance the photocatalytic performance because the photogenerated electrons and holes can migrate from the core to the shell to trigger water splitting or organic oxidation. However, the conventional type-II heterojunction may cause the retention of electrons or holes in the core, which will hinder their usage. On the other hand, the preparation of heteroatomic gradient-doped semiconductors to adjust the band structure has gained a lot of attention [6,7,17,18], because the gradually changed heteroatomic doping level may form a bent band structure at the gradient-doped layer, which can facilitate the charge separation. Therefore, constructing core-shell TiO_2@N-TiO_2 heterojunction with gradient-doped N level could be a fantastic way to improve the photocatalytic performance, which is rarely reported before.

Herein, a branched core-shell nanosphere composed of an anatase TiO_2 (a-TiO_2) core and a shell of gradient-doped N-TiO_2 nanobranches (a-TiO_2@N-TiO_2) is synthesized by an *in situ* doping process in the presence of $NH_3{\cdot}H_2O$ as N source for the first time. During the preparation process, a mixed crystal anatase-rutile TiO_2 (ar-TiO_2) nanosphere is first prepared by oxidizing Ti in H_2O_2 solution and then etched by $NH_3{\cdot}H_2O$ to form $(NH_4)_2TiO_3$ shell, which is further annealed in ambience to obtain the final product, a-TiO_2@N-TiO_2. The morphology of the samples could be modified by the amount of $NH_3{\cdot}H_2O$. The optimized a-TiO_2@N-TiO_2 with an uniform size of ~700 nm, including a ~500 nm core and a ~100 nm shell composed of gradient-doped N-TiO_2 nanobranches (the doping level gradually increased from the shell bottom to the shell surface), which exhibit narrowed band gap to improve the visible light response and form a n-n^+ heterojunction between the a-TiO_2 core and N-TiO_2 shell. Furthermore, the gradient-doped N should result in a bent band structure in the shell, which can also enhance the separation of photogenerated carriers, leading to a remarkably improved photocatalytic performance in both producing H_2 and degrading refractory organic pollutants.

The detailed synthesis process of branched core-shell a-TiO_2@N-TiO_2 nanosphere is illustrated in the Supporting information and Fig. 1a. In the first stage, H_2O_2 reacts with the Ti atoms on the surface of Ti foil (Eq. 1), leading to the generation of mixed crystal ar-TiO_2 nanospheres (Figs. S1 and S2 in Supporting information). As the time increased, $NH_3{\cdot}H_2O$ reacts with the outer TiO_2 on the surface of ar-TiO_2 microspheres to generate $(NH_4)_2TiO_3$ (Eq. 2) [19]. The reactions could be described as follows:

$$H_2O_2 + Ti \rightarrow TiO_2 + H_2O \quad (1)$$

$$TiO_2 + NH_3{\cdot}H_2O \rightarrow (NH_4)_2TiO_3 + H_2O \quad (2)$$

The reaction between Ti atoms and H_2O_2 forms a porous structure in the TiO_2 according to the Kirkendall effect (Fig. S2d) [19]. Meanwhile, $NH_3{\cdot}H_2O$ solutions corrode the TiO_2 on the surface, leading to the formation of core-shell structure with ar-TiO_2 as core and $(NH_4)_2TiO_3$ as shell. Under the effects of the H_2O_2 and $NH_3{\cdot}H_2O$, the surface of TiO_2 particle is corroded into a branched structure. After calcination, the ar-TiO_2 can be converted into anatase TiO_2 [20], while the $(NH_4)_2TiO_3$ can be turned into N-TiO_2 [21], and finally the 3D branched core-shell a-TiO_2@N-TiO_2 nanospheres are synthesized.

The morphologies of the as-prepared samples are first characterized by scanning electron microscopy (SEM). In the control experiments, various amount of $NH_3{\cdot}H_2O$ is used in the preparation process and different kinds of nanospheres are obtained (Figs. 1b–d and Fig. S3 in Supporting information) and denoted as a-TiO_2@N-TiO_2-x (x = 0, 2, 4, 6 and 8). However, the branched core-shell a-TiO_2@N-TiO_2 nanospheres can be synthesized with only 4 mL $NH_3{\cdot}H_2O$ (Figs. 1b-d), which display a structure of branched nanosphere with a uniform size distribution (Fig. 1b) and average diameter of ~700 nm (Fig. 1c). Fig. 1d depicts magnified SEM image of a single a-TiO_2@N-TiO_2–4 nanosphere. The surface of the nanosphere is composed of disorderly nanobranches with the length about ~50 nm, which significantly improves its surface area and the amount of active sites. The results of energy dispersive X-ray (EDX) mapping (Figs. 1e–g) confirm that the a-TiO_2@N-TiO_2 nanospheres consisted of Ti, O and N, demonstrating the existence of N. The X-Ray diffraction (XRD) plots (Fig. S4 in Supporting information) indicate that all these samples display highly crystallized structure with distinct characteristic peaks of anatase-phase TiO_2 (PDF #21–1272) [22], implying that the doping of N do not affect the crystalline phases of the TiO_2, and the ar-TiO_2 could be transferred into anatase TiO_2 completely after annealing.

The detailed morphologies and microstructures of a-TiO_2@N-TiO_2–4 are further investigated by transmission electron microscopy (TEM). Fig. 1h shows a typical TEM image of the a-TiO_2@N-TiO_2–4 nanospheres, in which the nanospheres are well-dispersed without aggregation and the average diameter is ~700 nm. Further magnified TEM image (Fig. 1i) clearly reveals a core–shell structure with a core diameter of ~500 nm and a shell thickness of ~100 nm. Based on the EDX line scan profile (insert in Fig. 1i), the EDX intensity of N element is gradually increased from the bottom of the shell to the edge, suggesting a gradient-doped N in the shell, which could result in a bent band structure in the shell to facilitate the separation of photogenerated charges [7]. However, the Ti and O elements show higher intensity than N element and slightly reduced from the core center to the edge, which demonstrates a structure of localized a-TiO_2 core and N-TiO_2 shell. The shell is consisted of a large number of nanocrystals, which form the nanobranches (Fig. 1j). Thanks to the interlaced nanobranches on the surface of a-TiO_2@N-TiO_2–4, the sample displays an ultrahigh average pore-diameter of 18.44 nm with a Brunauer–Emmett–Teller (BET) surface area of 123 m^2/g (Fig. S5 in Supporting information), so that much more accessible reaction sites can be exposed and the capture of the light can be improved. Fig. 1k shows a typical high-resolution TEM (HRTEM) image of a-TiO_2@N-TiO_2–4, which is taken on the edge of a single nanorods. The lattice spacing is 0.35 nm, corresponding to the (101) crystal plane of anatase TiO_2 [23]. Moreover, it should be noted that the lattice fringes become blurred and discontinuous at the edges of N-TiO_2, indicating that it is a defects-rich region [24]. This could be attributed to the formation of abundant V_o in the lattice of TiO_2 due to the high-ratio of doping N at the edge as mentioned above (insert in Fig. 1i). This amorphous N-TiO_2 may derive more reactive sites for water splitting [25,26].

X-ray photoelectron spectroscopy (XPS) measurement reveals the existence of Ti, O and N in the a-TiO_2@N-TiO_2–4 (Fig. 2a), which is consistent with the results of EDX. The high-resolution XPS spectrum of Ti 2p (Fig. 2b) of a-TiO_2@N-TiO_2–4 shows two evident peaks located at 458.5 and 464.0 eV, which are ascribed to Ti $2p_{3/2}$ and Ti $2p_{1/2}$, respectively, which are slightly red-shifted compared with that of a-TiO_2@N-TiO_2–0 [27]. This red-shift could be ascribed to the N doping in the nanobranches coating, be-

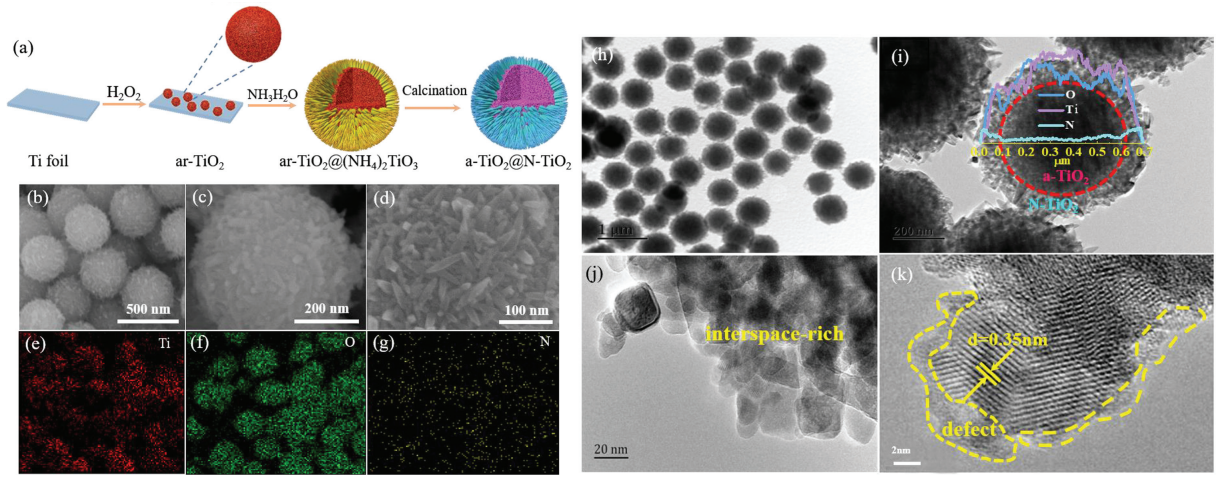

Fig. 1. (a) Schematic illustration of formation of branched core-shell a-TiO_2@N-TiO_2 nanosphere. (b-d) SEM images of the a-TiO_2@N-TiO_2–4, (e–g) EDX mapping of a-TiO_2@N-TiO_2–4 confirming the presence of Ti, O and N. TEM (h and i) and HRTEM (j and k) images of the a-TiO_2@N-TiO_2–4. Insert curves in (i) are the line scanning EDX results of the core-shell nanosphere.

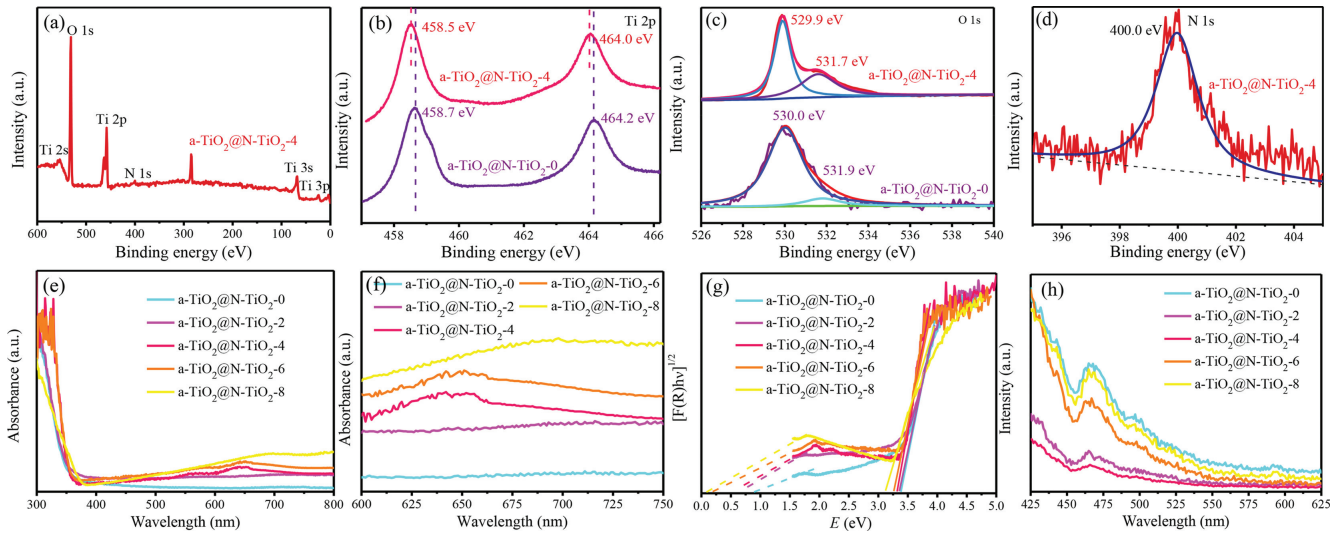

Fig. 2. (a) XPS spectrum of the a-TiO_2@N-TiO_2–4, (b) Ti 2p, (c) O 1s and (d) N 1s. (e) UV–vis, (f) enlarged UV–vis spectra (600–750 nm), (g) Tauc plot and (h) PL spectra of a-TiO_2@N-TiO_2-x (x = 0, 2, 4, 6 and 8).

cause the XPS mainly detects the sample's surface [24]. Fig. 2c shows the XPS spectra for O 1s region of a-TiO_2@N-TiO_2–0 and a-TiO_2@N-TiO_2–4. It can be seen that the a-TiO_2@N-TiO_2–0 shows a broad peak at 530.0 eV, which can be ascribed to the Ti–O-Ti in anatase TiO_2, while a small peak at 531.9 eV is attributed to the hydroxyl groups of the chemisorbed water [28]. However, the O 1s peak of a-TiO_2@N-TiO_2–4 can be split as two red-shifted peaks at 529.9 eV and 531.7 eV, respectively, which could also be attributed to the formation of abundant V_o and amorphous TiO_2 due to the N doping. The a-TiO_2@N-TiO_2–4 shows a weak peak at 400 eV ascribed to N 1s (Fig. 2d), which is in accordance with the doped N in TiO_2 as reported before [29]. The XPS results further demonstrate the a-TiO_2@N-TiO_2 nanospheres are anatase phase, and N is successfully doped in the sample by the facile *in situ* doping process.

Generally, doping with non-metallic elements, including N, and formation of V_o could alter the electronic properties of TiO_2. We therefore explore the electronic band structure of a-TiO_2@N-TiO_2-x using UV-DRS spectra. As shown in Fig. 2e, the visible light absorption of the a-TiO_2@N-TiO_2-x is significantly enhanced with the increase of the N content, indicating the N dopant can effectively narrow the band gap of TiO_2 and make it active under visible light. In addition, a-TiO_2@N-TiO_2-x also exhibit another obviously weak absorption band in the range from 600 nm to 750 nm (Fig. 2f), suggesting there is not a homogeneous distribution of N doping and V_o in the bulk a-TiO_2@N-TiO_2-x [24], and this is consistent with the TEM results. The corresponding band structures of the a-TiO_2@N-TiO_2-x are also calculated and shown in Fig. 2g. According to the transformed Kubelka-Munk function $\alpha h_\upsilon = A(h_\upsilon E_g)^{1/2}$, a gradually red shift of the band gaps (3.35, 3.31, 3.27, 3.25, 3.1 eV) of a-TiO_2@N-TiO_2-x are observed with the amount of $NH_3 \cdot H_2O$ increased, which is in accordance with their optical adsorption properties. It should be noted that, exception of the main band gaps, a-TiO_2@N-TiO_2-x (x = 2, 4, 6, and 8) have another weak band structures, which can be attributed to the existed impurity level and defect level [24,30,31]. In addition, the photoluminescence (PL) spectra are executed to evaluate the separation efficiency of photoexcited charge carriers in the samples. As displayed in Fig. 2h, a-TiO_2@N-TiO_2–4 shows the weakest PL intensity, indicating the fast electrons transfer between a-TiO_2 and N-TiO_2, which lead to the PL quenching and reduce the electron-hole recombination [32].

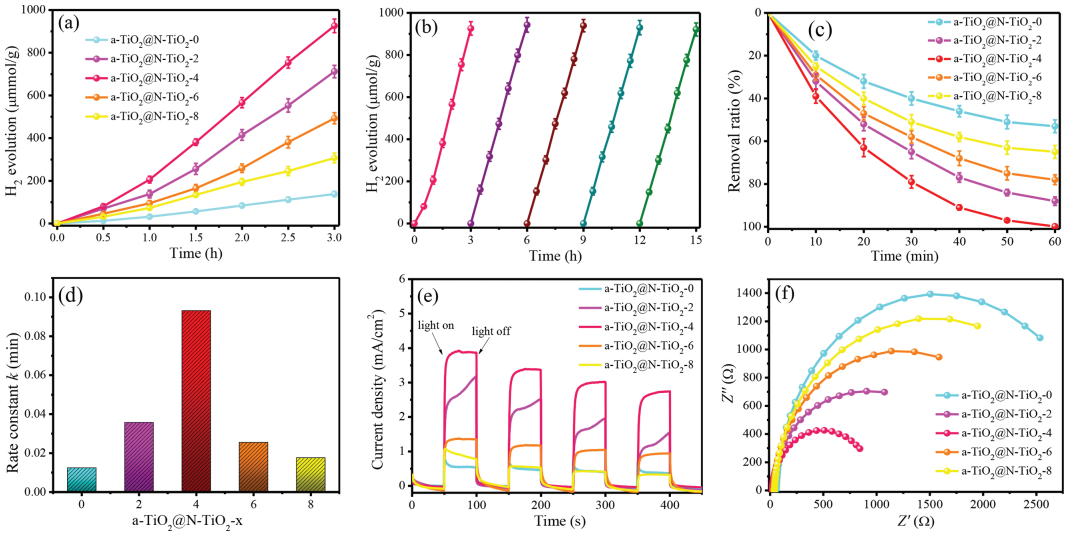

Fig. 3. (a) Hydrogen evolution of the samples and (b) recycled hydrogen evolution for 15 h of a-TiO_2@N-TiO_2–4 under AM 1.5 irradiation with 20 vol% methanol as the sacrificial agent. (c) Removal ratio and (d) rate constant on photocatalytic degradation of TC by a-TiO_2@N-TiO_2-*x* under AM 1.5 illumination (TC = 10 ppm, $T = 25$ °C). (e) Chopped *J-t* curves tested at 0.8 V *vs.* SCE under AM 1.5 illumination, and (f) EIS Nyquist plots of the a-TiO_2@N-TiO_2-*x*.

The photocatalytic H_2 production performance is evaluated under air mass (AM) 1.5 irradiation with 20 vol% methanol as the sacrificial agent (Figs. 3a and b). As displayed in Fig. 3a, the photocatalytic activity of a-TiO_2@N-TiO_2-*x* is enhanced with increasing N content from a-TiO_2@N-TiO_2–0 to a-TiO_2@N-TiO_2–4, which should be attributed to the enhanced charge transfer at the photocatalyst/solution interface due to the arising of nanobranches, and improved separation of photogenerated electron/hole pairs in the bulk phase ascribed to the formation of gradient N doping. The a-TiO_2@N-TiO_2–4 possesses the highest photocatalytic activity with the H_2 production rate of 308.1 μmol g^{-1} h^{-1}, which is superior to most of the TiO_2-based photocatalysts for H_2 production reported to date (Table S1 in Supporting information). However, a further increase of N content, the photocatalytic activity of a-TiO_2@N-TiO_2-*x* ($x = 6$ and 8) composites is decreased. This can be due to the excess O defects sites in a-TiO_2@N-TiO_2-*x*, which can also act as the recombination centers for the photogenerated electron/hole pairs [33]. Moreover, the superfluous $NH_3 \cdot H_2O$ would destroy the branched core-shell morphology (Figs. S3d-g in Supporting information), which is adverse for the separation and transportation of the charges. The stability of the a-TiO_2@N-TiO_2–4 photocatalyst is further evaluated (Fig. 3b). There is no evident photocatalyst deactivation in continuous H_2 evolution measurements after 15 h operation, which demonstrates the excellent stability of a-TiO_2@N-TiO_2–4 for photocatalytic H_2 evolution.

As one of the most active photocatalyst, the photogenerated holes of TiO_2 have enough oxidation potential (~3.1 V *vs.* Normal Hydrogen Electrode, NHE) to oxidize the absorbed hydroxyl into hydroxyl radicals and also directly oxidize most kinds of organics [34]. The photocatalytic performance is further evaluated by degrading tetracycline (TC) under AM 1.5 illumination (Figs. 3c and d). The results indicate that the a-TiO_2@N-TiO_2–4 shows the highest active in removing TC, which can remove almost 100% TC from the solution after 1 h operation with a rate constant (k) of ~0.093 min^{-1} (Fig. S6 in Supporting information). The ranking of activity of these samples are the same as the photocatalytic H_2 evolution, which further demonstrates the optimized sample is a-TiO_2@N-TiO_2–4. The active species in the TC degradation process are studied using the trapping experiments. As shown in Fig. S7 (Supporting information), $^{\cdot}OH$ and h^+ are the main active species in the degradation of TC. In the photocatalytic degradation process, organics can be oxidized by the holes and the corresponding hydroxyl radicals [35], which means the photocatalytic activity is mainly determined by the separation efficiency of the photogenerated electron/hole pairs in the photocatalyst. So, the ranking of activity is the same in both photocatalytic water splitting and organic decomposition.

The photocatalytic activity of a-TiO_2@N-TiO_2–4 is further investigated by removing various refractory organic pollutants (Table S2 in Supporting information), including organic dyes, phenols, antibiotics, and personal care products (PCPs). Excellent removal ratios are achieved for these model pollutants after 1 h or 2 h operation under AM 1.5 illumination. The removal ratios of the organic dyes are higher than 91% after 1 h operation even with an initial concentration of 20 ppm, which are much higher than that of others. This should be due to the relatively easy fading of organic dyes. The removal rates of phenols are relatively smaller than others, lower than 90% after 1 h operation with an initial concentration of 10 ppm, which should be attributed to their more stable molecular structures than other model pollutants. However, after 2 h operation, all these organic pollutants could be degraded over 96%, and the removal ratios of total organic carbon (TOC) are similar and reach to 65.8%–77.3% after 5 h operation, which further demonstrates the outstanding photocatalytic performance of a-TiO_2@N-TiO_2–4 in degrading organic pollutants.

To confirm the enhanced charge separation efficiency in the branched core-shell a-TiO_2@N-TiO_2 nanospheres, chronoamperometry (*J-t*) and electrochemical impedance spectroscopy (EIS) measurements are carried out for all as prepared samples. As shown in Fig. 3e, all samples show transient photocurrent response when turn on the light, which further demonstrates all of them have photoactivity. A higher photocurrent response means a more efficient charge separation performance. The a-TiO_2@N-TiO_2–4 shows the highest photocurrent density compared with others, which indicates the optimized morphology of nanobranched core-shell nanosphere and gradient N doping significantly enhance the charge transfer and separation. Furthermore, the a-TiO_2@N-TiO_2–4 presents a representative EIS Nyquist plot with a much smaller arc radius than that of other samples (Fig. 3f), which means that the charge transfer resistance is remarkably decreased by the appropriate doping of N in a-TiO_2@N-TiO_2–4. In general, both *J-t* and ESI results reveal the high efficiency of a-TiO_2@N-TiO_2–4 in accelerating charge transfer and separation, and thus an excellent photocatalytic performance could be anticipated.

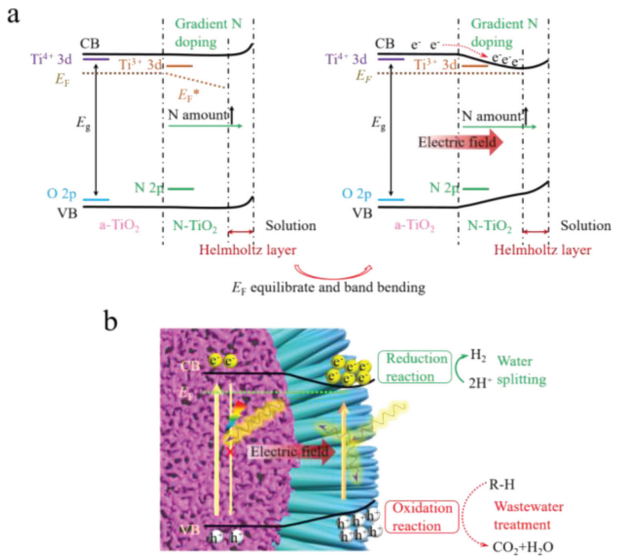

Fig. 4. Schematic illustration of (a) the band structure evolution for the formation of homojunction and (b) photoexcited carrier transfer in the branched core-shell a-TiO_2/N-TiO_2 nanospheres with a gradient distribution of N element in the nanobranches.

Based on the above analyses, we propose the possible energy levels and charge transfer pathways in the branched core-shell a-TiO_2@N-TiO_2 nanospheres and show them in Fig. 4. In the darkness, the E_F of N-TiO_2 would be lower than that of a-TiO_2 because the existed impurity level induced by N doping (left part of Fig. 4a) [14]. As the doping amount of N increasing from the bottom of the branched shell to the surface, the E_F should decrease gradually [16]. Therefore, the electrons in the a-TiO_2 would transfer to the N-TiO_2, which could lead to the equilibration of E_F and the band bending in the gradient N doped branch layers, forming a n-n^+ heterojunction with unique band structure (right part of Fig. 4a). Furthermore, the migration of electrons could cause the formation of electric field between a-TiO_2 and N-TiO_2. In this situation, both photogenerated electrons and holes can be driven to the conduction band (CB) and valence band (VB) of N-TiO_2 nanobranches, respectively. In the presence of hole scavengers, the charge recombination will be effectively suppressed in the N-TiO_2 nanobranches, therefore the evolution of H_2 can be significantly enhanced by the reduction of electrons. When applying in photocatalytic wastewater treatment, the holes should oxidize the absorbed organics directly, or oxidize the absorbed –OH groups into hydroxyl radicals ($^{\cdot}OH$) for further oxidizing organics efficiently, while the electrons should be captured by dissolved oxygen for oxygen reduction reaction (ORR) [34]. Obviously, this unique band structure and charge transfer model is very applicable in this core-shell heterojunction for hindering charge recombination, because both electrons and holes can be applied in reduction and oxidation reactions efficiently at the photocatalyst/solution interface (Fig. 4b). Furthermore, the ultrathin amorphous layer at the nanobranches′ surface (Fig. 1k) can enhance the absorption of substances and provide more active sites [17], therefore facilitating the charge transfer at the photocatalyst/solution interface. In addition, the nanobranches should cause the reflection of light, enhancing the light harvesting for producing more charges. Consequently, the branched core-shell a-TiO_2@N-TiO_2 nanospheres with gradient N doping show significantly improved photocatalytic activities in both solar water splitting and wastewater treatment.

In general, we synthesize a novel branched core-shell a-TiO_2@N-TiO_2 nanosphere with a gradient N doping in the nanobranches for highly efficient photocatalytic hydrogen generation and wastewater purification. The nanosphere is prepared by a facile wet chemical method, in which the amount of $NH_3{\cdot}H_2O$ plays an important role to control the nanosphere's morphology. The optimized amount is 4 mL in the given conditions, and the obtained nanospheres has uniform morphology with a mesoporous core of a-TiO_2 (~500 nm of diameter) and a shell of N-TiO_2 nanobranches with gradient N doping (gradually increased from the bottom to the top, ~100 nm of thickness) and a ultrathin amorphous coating. This optimized sample shows a H_2 production rate of 308.1 μmol h^{-1} g^{-1} under AM 1.5 illumination, which is about 6.7 times higher than that of the bare TiO_2 nanosphere. Furthermore, the a-TiO_2@N-TiO_2 nanospheres also exhibit high activity in removing various refractory organic pollutants. The outstanding photocatalytic performances of the a-TiO_2@N-TiO_2 nanosphere should be attributed to the following reasons: (1) the gradient N doping cause the formation of n-n^+ heterojunction and electric field between a-TiO_2 and N-TiO_2, which drive photogenerated electrons and holes transferring to the N-TiO_2 nanobranches; (2) the ultrathin amorphous layer at the nanobranches' surface enhance the absorption of substances and provide more active sites; (3) the nanobranches cause the reflection of light, enhancing the light harvesting for producing more charges. This work provides a significant reference for the rational design of unique nanostructured photocatalyst used in hydrogen production and wastewater purification.

Declaration of competing interest

The authors declare no conflict of interest.

Acknowledgments

This research was supported by the National Natural Science Foundation of China (No. 52170083), the Excellent Youth Fund Project of Natural Science Foundation of Hunan Province (No. 2021JJ20007), and the Research Foundation of Education Bureau of Hunan Province, China (No. 21B0441).

Supplementary materials

Supplementary material associated with this article can be found, in the online version, at doi:10.1016/j.cclet.2022.06.051.

References

[1] Q.S. Zhang, Y.M. Li, H. Ren, et al., Chem. Eng. J. 408 (2021) 127267.
[2] H.D. Ji, J.R. Ni, D.Y. Zhao, et al., ACS EST Eng. 2 (2022) 1015–1038.
[3] Q.S. Zhang, Y. Xiao, Y.M. Li, et al., Chem. Eng. J. 393 (2020) 124681.
[4] Y.C. Zhou, P. Wang, H. Fu, et al., Chin. Chem. Lett. 31 (2020) 2645–2650.
[5] X.N. Liu, H.D. Ji, S. Li, et al., Chemosphere 233 (2019) 198–206.
[6] H.D. Ji, W. Liu, F.B. Sun, et al., Chem. Eng. J. 419 (2021) 129605.
[7] A. Mirzaei, M. Eddah, S. Roualdes, et al., Chem. Eng. J. 422 (2021) 130507.
[8] R. Asahi, T. Morikawa, T. Ohwaki, et al., Science 293 (2001) 269–271.
[9] M. Esmat, H. El-Hosainy, R. Tahawy, et al., Appl. Catal. B 285 (2021) 119755.
[10] S. Livraghi, M.C. Paganini, E. Giamello, et al., J. Am. Chem. Soc. 128 (2006) 15666–15671.
[11] R. Asahi, T. Morikawa, H. Irie, et al., Chem. Rev. 114 (2014) 9824–9852.
[12] D.N. Zhang, X.Y. Ma, H.W. Zhang, et al., Mater. Today Energy 10 (2018) 132–140.
[13] A.K. See, R.A. Bartynski, J. Vac. Sci. Technol. A 10 (1992) 2591–2596.
[14] M.A. Henderson, W.S. Epling, C.H.F. Peden, et al., J. Phys. Chem. B 107 (2003) 534–545.
[15] K. Wang, T. Peng, Z.M. Wang, et al., Appl. Catal. B 250 (2019) 89–98.
[16] X.S. Huang, Z.M. Gao, P. Li, et al., J. Appl. Phys. 123 (2018) 084502.
[17] C.X. Li, S.H. Dong, R. Tang, et al., Energy Environ. Sci. 11 (2018) 3201–3211.
[18] J.Y. Kim, G.C. Liu, R.E.A. Ardhi, et al., Nano-Micro Lett. 14 (2022) 46.
[19] C.X. Wang, L.W. Yin, L.Y. Zhang, et al., Langmuir 26 (2010) 12841–12848.
[20] W.W. Fu, G.D. Li, Y. Wang, et al., Chem. Commun. 54 (2018) 58.
[21] D.H. Chen, F.Z. Huang, L. Cao, et al., Chem. Eur. J. 43 (2012) 13762–13769.
[22] Q.Y. Zeng, S. Chang, A. Beyhaqi, et al., Nano Energy 67 (2020) 104237.
[23] M.H. Wu, Y.P. Gao, Y. Hu, et al., Chin. Chem. Lett. 31 (2020) 897–902.
[24] X.Q. Hao, Y.C. Wang, J. Zhou, et al., Appl. Catal. B 221 (2018) 302–311.
[25] X. Hu, C. Li, J. Song, et al., J. Colloid Interf. Sci. 574 (2020) 61–73.
[26] C.T. Feng, P.F. Wu, Q.L. Li, et al., New J. Chem. 46 (2022) 1731–1740.

[27] J.H. Park, S. Kim, A.J. Bard, Nano Lett. 6 (2006) 24–28.
[28] W.C. Wang, Z.X. Yang, G.Y. Li, et al., J. Alloys Compd. 890 (2021) 161895.
[29] S. Khan, T.L. Ruwer, N. Khan, et al., J. Mater. Chem. A 9 (2021) 12214.
[30] X.Q. Hao, Z.W. Cui, J. Zhou, et al., Nano Energy 52 (2018) 105–116.
[31] S.M. Zhu, X.J. Qian, D.P. Lan, et al., Appl. Catal. B 269 (2020) 118806.
[32] S. Sun, P. Gao, Y. Yang, et al., ACS Appl. Mater. Interfaces 8 (2016) 18126–18131.
[33] M. Kong, Y.Z. Li, X. Chen, et al., J. Am. Chem. Soc. 133 (2011) 16414–16417.
[34] Q.Y. Zeng, S. Chang, A. Beyhaqi, et al., J. Hazard. Mater. 394 (2020) 121–425.
[35] Q.Y. Zeng, S. Chang, M. Wang, et al., Chin. Chem. Lett. 32 (2021) 2212–2216.